Article

Ultra-low core loss in Fe-enriched soft magnetic ribbons enabled by nanostructure and high-frequency domain engineering

Ravi Gautam [1], Shozo Hiramoto[2], Nikita Kulesh[1], Hiroaki Mamiya [1], Satoshi Okamoto[1,2], Nobuhisa Ono[2], Takeshi Ogasawara[3], Tadakatsu Ohkubo [1] & Hossein Sepehri-Amin [1] ✉

The next generation of power electronics necessitates materials capable of rapid response at tens of kilohertz frequencies while ensuring minimal core losses. Accelerating the advancement of power electronics hinges on addressing the current shortage of ultra-low core loss soft magnets, thereby enabling sustainable energy utilization and paving the way toward achieving zero carbon footprints. Here we demonstrate an approach that integrates nanostructure engineering with high-frequency domain structure control, significantly enhancing the performance of Fe-enriched amorphous ribbons. Our strategy reduces core loss by 55%, achieving an ultra-low loss of ~ 75 ± 1.3 W/kg at 10 kHz, 1 T. We attribute this improvement to optimized perpendicular magnetic anisotropy, which is induced by positive magnetostriction and compressive stress generated from partial nanocrystallization of α-Fe in a residual amorphous matrix. These configurations lead to the formation of a narrow stripe-shaped magnetic domain (~ 4.8 ± 0.6 μm wide), resulting in minimal excess loss. These findings highlight a pivotal advancement in soft magnet design, facilitating energy-efficient, miniaturized power electronics for modern applications.

Demand for next-generation power electronic devices is surging due to their essential roles in AI-driven automation, robotics, electric vehicles, renewable energy systems, and smart grids. Recent advancements in wide-bandgap semiconductors, such as SiC and GaN, have significantly boosted the efficiency and miniaturization of modern power electronic devices[1]. However, the increased switching frequencies enabled by these semiconductors are placing new demands on soft magnetic materials for compact and efficient transformers, inductors, and other electromagnetic devices. Magnetic passive devices are estimated to account for over 50% of losses in the power electronic systems[2]. Therefore, the advancement of these devices would be accelerated by the development of soft magnets that possess high saturation magnetization $\mu_0 M_s$, low coercivity H_c, high electrical resistivity ρ, and minimal core loss P_T at high switching frequencies[3–6].

The main challenge in developing soft magnetic materials lies in resolving the trade-offs among achieving high $\mu_0 M_s$, low H_c, and low P_T. Applications such as transformers and magnetic actuators prioritize high $\mu_0 M_s$ to enable compact, high-flux designs, whereas high-frequency devices like EV inverters and power supplies demand materials with low P_T to improve efficiency and thermal stability[7]. Efforts to reduce P_T in widely used Si-steel alloys through increased Si content[8], alloying strategies[9], and microstructural refinements[10–13] have led to marginal improvements, reaching a performance plateau with high P_T at elevated frequencies, rendering them unsuitable for cutting-edge applications. Other conventional alloys also encounter similar issues with substantially high losses[9,14–16], while soft ferrites, despite attaining minimal P_T, are constrained by inadequate power density, increasing copper loss, and limiting their applicability[17]. Fe-

[1]National Institute for Materials Science (NIMS), Tsukuba, Japan. [2]Institute of Multidisciplinary Research for Advanced Materials (IMRAM), Tohoku University, Sendai, Japan. [3]National Institute of Advanced Industrial Science and Technology (AIST), Tsukuba, Japan. ✉e-mail: h.sepehriamin@nims.go.jp

based amorphous and nanocrystalline materials, such as FINEMET[18], NANOPERM[19,20], and VITROPERM[21,22], offer lower P_T due to the exchange-averaging effect of local anisotropy. However, these typically exhibit low $\mu_0 M_s$ (1.2–1.5 T) and contain expensive elements. Recent advancements have increased $\mu_0 M_s$ to 1.8–2 T by raising the Fe content in nanocrystalline soft magnets[23–29]. Nevertheless, achieving an optimal balance of magnetic properties, particularly reducing P_T at high frequencies, remains a bottleneck. Core loss comprises hysteresis loss P_h, classical eddy current loss P_e, and excess loss P_a[30]. Addressing these losses becomes more significant as the frequency increases[31,32]. At low frequencies, the dominant component is typically P_h, which originates from the irreversible motion of domain walls and is influenced by magnetic properties such as H_c and domain wall movement. As the frequency increases, P_e, which arises from Joule heating caused by eddy currents, becomes more significant and scales with the square of the frequency. This can be mitigated by enhancing ρ and reducing specimen thickness. At even higher frequencies, P_a, associated with domain wall dynamics, becomes increasingly important and can be reduced by narrowing magnetic domains and increasing domain wall density to decelerate domain wall motion during AC magnetization. However, understanding the intrinsic and extrinsic contributions to core losses, especially P_a, for high-frequency regimes, is still limited. Theoretically, it has been proposed that inducing weak perpendicular magnetic anisotropy (PMA) through internal stresses in amorphous material with positive magnetostriction λ_s may minimize losses[33–37]. However, approaches such as surface oxidization are technically difficult to apply to real magnetic devices. Therefore, the practical implementation of this theory would require precise nanostructure engineering to fine-tune the magnetic domain structure. This method can serve as a strategic framework for designing advanced soft magnetic materials.

In this study, we propose and demonstrate a new approach to significantly reducing P_T in soft magnetic materials at high frequencies through controlled nanostructure and magnetic domain engineering. Our versatile strategy broadly applies to various Fe-based amorphous systems, highlighting its universal applicability. We developed Fe-rich amorphous ribbons with a high $\mu_0 M_s$ of 1.6 T by incorporating over 84 at.% Fe with cost-effective elements, ensuring economic viability. The $Fe_{84.8}Si_{0.5}B_{9.4}P_{3.4}Cu_{0.8}C_{1.1}$ (at.%) alloy was systematically designed to achieve high $\mu_0 M_s$ while ensuring amorphous phase stability and thermal processability[23–26]. High Fe content enhances $\mu_0 M_s$, whereas B, P, and C stabilize the amorphous structure. Si and P broaden the supercooled liquid region, facilitating controlled nanocrystallization. Cu promotes the heterogeneous nucleation of α-Fe nanocrystals, while P and C inhibit grain growth and improve casting stability. These features collectively enable the control of the nanocrystallization of α-Fe

in residual amorphous matrix to obtain a high-performance material for high switching frequencies. By reducing domain wall pinning sites and leveraging nanoscale grains within the exchange length[21,38], we achieved low H_c and minimal P_h losses. Additionally, P_e was suppressed by employing thin ribbons with an amorphous or partially nanocrystalline structure, inherently limiting eddy current pathways. Importantly, we demonstrate that P_a, a dominant loss component at high frequencies, can be effectively controlled by nanostructure engineering through short-duration annealing near the crystallization temperature, as schematically illustrated in Fig. 1. Our advanced soft magnet design concept comprises three distinct stages (Fig. 1): (a) fabrication of Fe-enriched amorphous ribbons, which exhibit wide, curvilinear magnetic domains originating from random internal stresses, resulting in high core losses. (b) Partial nanocrystallization of α-Fe in the residual amorphous matrix induces compressive stresses that generate weak PMA. This leads to the formation of stripe-shaped magnetic domains, significantly suppressing domain wall motion and drastically reducing core loss. (c) As the crystalline volume fraction increases further, finer stripe domains with higher anisotropy energy develop, which increases core loss but provides insight into the tunability of magnetic properties. The trade-off between $\mu_0 M_s$ and P_T observed across the annealing stages presents opportunities for application-specific material design. High-crystallinity structures with enhanced $\mu_0 M_s$ are promising for pulsed power, distribution transformers, and surge absorbers, while partially crystalline states with minimal losses are better suited for high-frequency transformers, EMI filters, and shielding applications. By facilitating the formation of PMA with a stripe-domain structure through nanostructure engineering, our integrated approach achieves a remarkable 55% reduction in core loss. This study not only advances the frontier of soft magnetic material design but also sets a new performance benchmark for modern applications. Comprehensive core loss analysis using conventional empirical models[15,30,39,40] and magnetization process decomposition model[32,41] has elucidated the dominant excess loss component and revealed a transition in the magnetization reversal mechanism from domain wall motion to magnetization rotation. This strategy paves the way for developing next-generation soft magnetic materials with high efficiency for high-frequency applications, with potential applicability to a wide range of Fe-based amorphous systems.

Results

Fe-enriched amorphous ribbons were fabricated using an industrial-scale rapid solidification process, demonstrating excellent quality and flexibility (Methods and Supplementary Fig. 1), which were originally designed as well-nanocrystalline material[26]. These ribbons are 60 mm wide, $25 \pm 1 \mu m$ thin and several hundred meters long, showcasing the
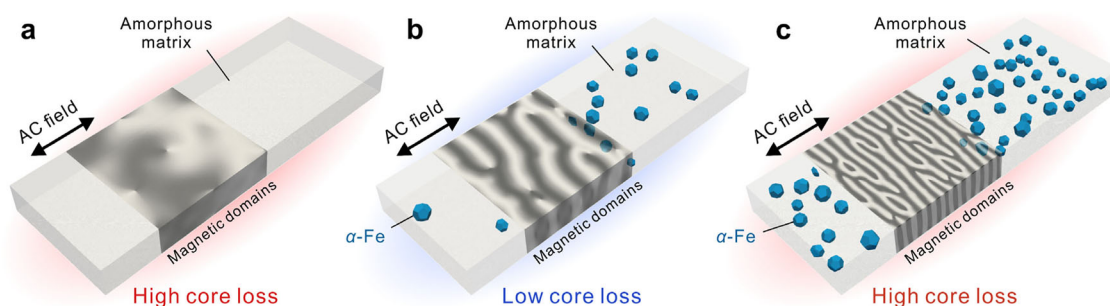
Fig. 1 | Schematic representation of performance enhancement in Fe-enriched amorphous ribbons through nanostructure and magnetic domain engineering. The schematic illustrates our strategic approach in designing ultra-low core loss soft magnetic material. This highlights the correlation between the performance of Fe-enriched amorphous ribbon and changes in microstructure and magnetic domain configurations. The phenomena are depicted in three distinct scenarios: **a** as-spun Fe-enriched amorphous ribbons exhibit broad, curvy magnetic domains, resulting in high heat dissipation; **b** with the emergence of partial nanocrystallization of α-Fe in the residual amorphous matrix, a transformation to striped magnetic domain occurs, significantly reducing heat dissipation; and **c** a high volume fraction of nano-scale α-Fe crystals forms in a residual amorphous matrix, accompanied with compact, narrow striped magnetic domains, leading to increased heat dissipation.

industrial scalability at low manufacturing and raw material costs. Differential scanning calorimetry (DSC) of the as-spun (As-Q) ribbons revealed crystallization of α-Fe and Fe-compound phases at onset temperatures of $T_{x1} = 667$ K and $T_{x2} = 795$ K, respectively (Supplementary Fig. 2). A large ΔT ($= T_{x1} - T_{x2} = 128$ K) provides a broad annealing window to control the crystallinity of the α-Fe phase within the residual amorphous matrix, inhibiting the complex phases that can degrade the properties[21]. Consequently, the as-spun ribbons were annealed at temperatures ranging from 573 to 748 K (Methods and Supplementary Table 1), producing samples with different crystalline volume fractions V_f (Supplementary Fig. 3) while maintaining crystallite size below the exchange length (~30–40 nm)[28,42,43] to avoid cubic magneto-crystalline anisotropy that would impair soft magnetic properties[21]. X-ray diffraction (XRD) analysis (Supplementary Fig. 4) confirmed a clear transition from amorphous to crystalline structures, with sharper and more intense peaks in highly crystalline samples and broader peaks in more amorphous ones. The as-spun ribbons exhibited a broad halo peak, indicating a fully amorphous phase, while α-Fe phases were consistently present with increasing V_f as the annealing temperature rose (Supplementary Table 1). A comprehensive investigation of the soft magnetic properties as a function of V_f revealed significant correlations with nanocrystallization (Fig. 2). It can be observed from Fig. 2a that the $\mu_0 M_s$ increase from 1.59 to 1.76 T as V_f rises, explained through the relationship, $\mu_0 M_s = \mu_0 M_{amo}(1 - V_f) + \mu_0 M_{cry} V_f$, where $\mu_0 M_{amo}$ and $\mu_0 M_{cry}$ are the saturation magnetization of the amorphous and crystalline phases, respectively. Since α-Fe has a higher magnetization than the residual amorphous matrix[15], overall magnetization increases with crystallinity. Figure 2b indicates no significant change in H_c with increasing V_f, with slight variations attributed to structural relaxation and crystalline phase emergence during annealing. Furthermore, Fig. 2c, d demonstrates that the λ_s and ρ of the samples remain relatively stable with V_f up to 10 %, after which both decreased, likely due to the diminishing amorphous regions as per the rule of mixtures. Figure 2e highlights that the size of the nanocrystals formed in the amorphous matrix remains below 20 nm across all samples, which is significantly smaller than the domain wall width[21], effectively preventing the pining effect and exhibiting low coercivity.

The investigation of core loss P_T at 10 kHz and a peak induction B_m of 1 T provided significant insights into how nanostructure engineering can minimize losses and improve the material's suitability for high-frequency applications. Notably, partial nanocrystallization of the α-Fe phase drastically reduces P_T, as shown in Fig. 2f. The as-spun ribbons exhibited a P_T value of 165.8 ± 0.84 W/kg, which decreased remarkably to 75 ± 1.3 W/kg, representing ~55% reduction in P_T within a V_f range of 0.5–6%. Beyond this range, P_T increased, emphasizing the importance of maintaining partial nanocrystallization for minimal P_T. Typically, the V_f value for conventional soft magnetic nanocrystalline materials is around 50%, and the very low V_f region has been paid little attention. This significant reduction in P_T underscores the potential for nanostructure engineering to develop ultra-low core loss soft magnets, enhancing their usability for high-frequency applications. A detailed analysis of core loss components was performed to understand the influence of physical parameters and to devise a nanostructure engineering strategy to minimize each component. It was found that component P_a is the dominant contributor to total loss (Fig. 2f), accounting for over 80%, while P_h and P_e together contributed less than 20% (Fig. 2b, d). P_h is minimal due to low H_c value, while P_e remains low because of the current material's advantageous combination of high ρ and low thickness. Notably, both loss components were over an order of magnitude smaller than the P_T at 10 kHz. It is widely accepted that P_a arises from non-uniform localized micro-eddy current induced by dynamic domain wall displacements, which depend on microstructural and domain features. Recent simulations suggest that λ_s can lead to core losses by dissipating magnetic energy into elastic energy[44,45]. Despite maintaining a relatively large

λ_s ~30 ppm across a V_f below 6% (Fig. 2c), P_T significantly drops, indicating a fundamentally different loss mechanism compared to conventional soft magnetic materials. P_a decreases with increasing V_f up to 6%, then increases beyond this range, aligning with the optimal V_f for minimal core loss. To understand the core loss behavior across the varying operating conditions, we extended the core loss analysis to a broad frequency range of 0.1–20 kHz at a fixed induction of 1 T. As shown in Supplementary Fig. 5, the core loss remains minimal for the partially nanocrystalline region (0.5–6%) across all operating frequencies, consistent with the trend observed at 10 kHz. The relative contributions of the individual loss components also evolve systematically with frequency: P_h dominates at lower frequencies, while P_a becomes the primary contributor beyond ~1 kHz. P_e remains relatively small and nearly constant due to the high resistivity and thin geometry of the ribbons. These observations further confirm the proposed method of magnetic domain engineering via PMA in samples with partial nanocrystallization of α-Fe ($V_f \approx 1$–6%), which yields minimal core loss at elevated frequencies. This analysis reinforces the robustness of this nanostructure-engineered approach in minimizing P_a. Further, the magnetization process decomposition model was employed to analyze both the as-spun and a low core loss sample annealed at 697 K (L-CL), to gain a better understanding of the core loss mechanism[32,41]. Broadband complex permeability (μ' and μ'') and core loss per cycle P_c were measured at various B_m and frequencies f ("Methods" and Supplementary Fig. 6). P_c was found to increase steadily with f, showing a significant rise for frequencies higher than 10 kHz. Notably, the L-CL sample exhibited lower core loss compared to the as-spun sample, consistent with conventional core loss measurements. The decomposition analysis revealed that irreversible magnetization processes dominate at lower frequencies, while reversible processes become more prominent at higher frequencies. These findings suggest that the substantial increase in core loss at high frequencies (> several tens of kHz) is interpreted as P_a in our conventional empirical models, and the low core loss at frequencies ≤ 20 kHz can be due to a significant reduction of the loss component of the irreversible magnetization process corresponding to P_a.

Figure 3 provides an in-depth nanostructural analysis and compositional characteristics of Fe-rich soft magnetic ribbons, focusing on the correlation of nanostructural features and core loss variation. We focus on three distinct samples representing different regions on the core loss spectrum: as-spun, low core loss (L-CL), and a high core loss sample annealed at 746 K (H-CL). Low-magnification bright-field TEM (BF-TEM) images of the as-spun ribbons (Fig. 3a.i.) display homogeneous contrast, indicative of a uniform supersaturated solid solution. This structural homogeneity is further confirmed by high-resolution BF scanning TEM (STEM) images (Fig. 3a.ii). The corresponding selected area electron diffraction and nanobeam diffraction patterns displayed in the insets show characteristic halo rings, confirming the amorphous structure. In contrast, TEM images of the L-CL samples (Fig. 3b.i., b.ii.) reveal the emergence of nanoscale α-Fe crystals with an average size of 15.9 ± 3.9 nm dispersed within the amorphous matrix. H-CL ribbons (Fig. 3c.i., c.ii.) exhibit a higher volume fraction of crystalline phases, with a crystallite size of 18.1 ± 5.4 nm. High-resolution BF-STEM of both L-CL and H-CL samples highlights the distinct separation of α-Fe crystals by the residual amorphous matrix. Additional TEM images and α-Fe crystallite size distribution for selected samples are provided in Supplementary Figs. 7 and 8. Notably, the crystallite sizes remain below 20 nm across all samples, consistent with XRD analysis. As core loss escalates from L-CL to H-CL, the volume fraction of crystalline phases within the amorphous matrix also rises, contrasting with conventional nanocrystalline materials like FINEMET[18], NANOPERM[19,20], VITROPERM[21,22], and recent Fe-enriched nanocrystals[24,25,27–29,46].

Further nano-scale compositional information was obtained through APT. Figure 3d–f displays APT elemental maps for B, Cu, P, and
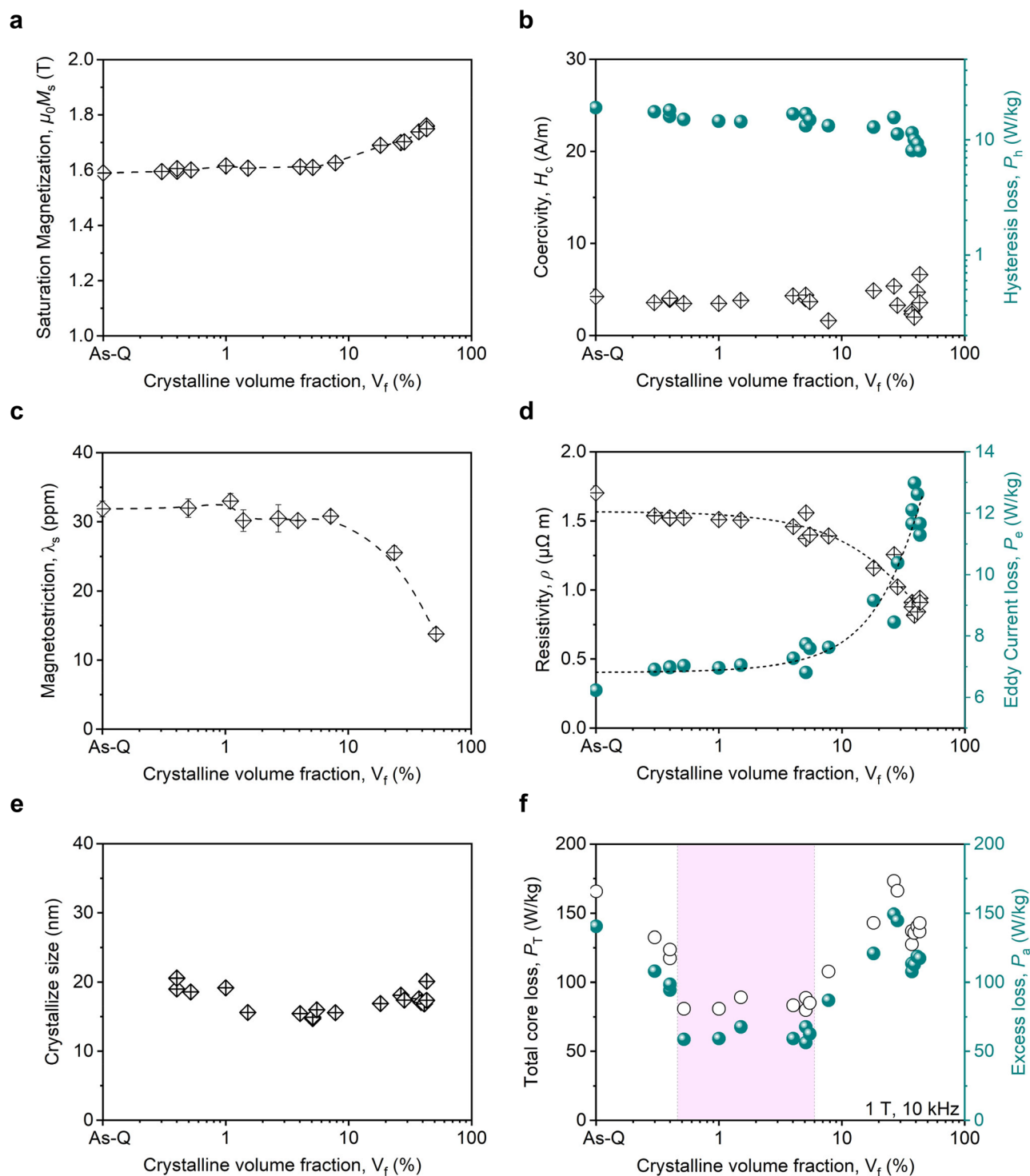
Fig. 2 | Evaluation of magnetic properties with varying crystalline volume fraction in Fe-enriched amorphous ribbon. a Saturation magnetization $\mu_0 M_s$ **b** coercivity H_c and hysteresis loss P_h, **c** magnetostriction λ_s, **d** resistivity ρ and corresponding eddy current loss P_e, **e** Crystallite size, and **f** Total core loss P_T along with excess loss P_a are plotted against the crystalline volume fraction in Fe-enriched amorphous ribbons.

Si with the corresponding concentration frequency distributions shown in Supplementary Fig. 9. A binomial (random) distribution is plotted to compare with the experimental concentration distributions of Cu, C, P, B, and Fe. The APT maps display ~10 nm thin slices, and compositional line profiles (Fig. 3g–i) indicate a homogeneous and random elemental distribution in as-spun ribbons, consistent with their amorphous structure. Notably, the experimental distribution of L-CL and H-CL samples deviates significantly from the binomial distribution, indicating non-uniform element arrangement and underlying ordering. 3D elemental maps (Fig. 3e, f) reveal α-Fe crystal nucleation within the amorphous matrix and a large number density of Cu clusters, acting as heterogeneous nucleation sites[47]. B and P lean regions correspond to α-Fe nanocrystals. The tendency of the size distribution of α-Fe nanocrystals in the APT maps is consistent with the XRD and TEM estimates. Further compositional analysis indicates that the nanocrystals are Fe-enriched with minor
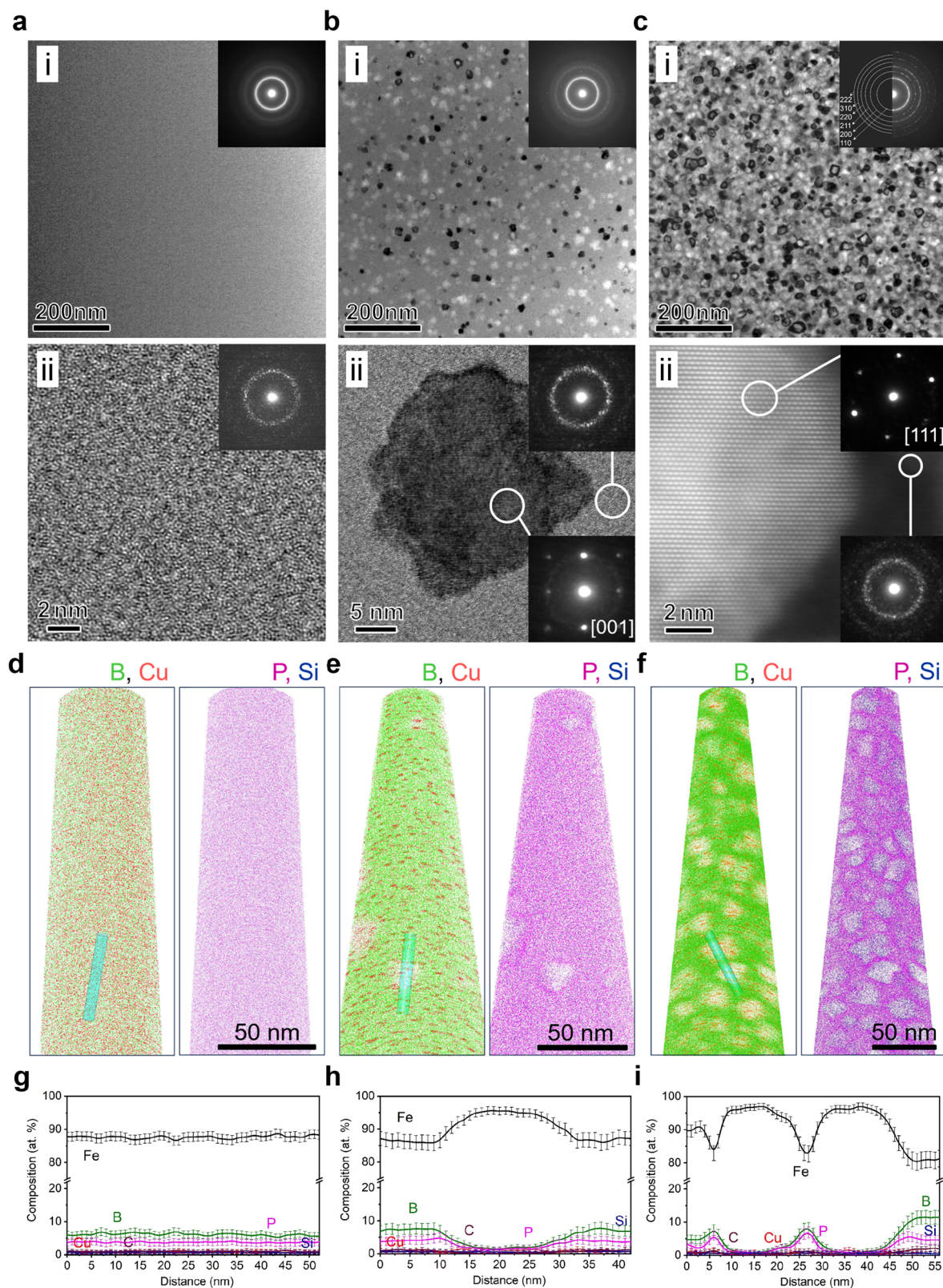
traces of other elements. Detailed compositions of the crystals and residual amorphous matrix for all three samples, calculated from compositional line profiles, are provided in Supplementary Table 2. The data shows a significant increase in the volume fraction of α-Fe nanocrystals, V_f, from 3.2% in L-CL to 26.3% in H-CL. This increase in V_f and Fe concentration in the crystalline phase accounts for the rise in $\mu_0 M_s$ values with increased crystallinity. Additionally, APT suggests

potential intrinsic property changes due to localized compositional variation.

To elucidate the mechanism behind core loss reduction in the very low V_f range of 0.5–6% compared to conventional nanocrystalline materials, while maintaining high λ_s, it is essential to analyze the shape and response of magnetic domains under a high-frequency AC-magnetic field. Therefore, we employed an advanced high-frequency

Fig. 3 | Microstructural and nano-scale compositional analysis of Fe-enriched soft magnetic ribbons. TEM images of **a** as-spun, **b** L-CL (annealed at 698 K), **c** H-CL (annealed at 746 K) samples. Each sample features a low-resolution bright-field image with an inset of corresponding SAED patterns shown in respective (i) and a high-resolution bright-field STEM image with an inset of corresponding nanobeam electron diffraction shown in respective (ii). The TEM images reveal an amorphous structure in the as-spun sample and the formation of nano-scale α-Fe crystals within a residual amorphous matrix in the annealed samples. APT elemental maps highlight B (green), Cu (orange), P (pink), and Si (blue) for the distinct samples: **d** as-spun, **e** L-CL, **f** H-CL. These maps show a uniform elemental distribution in the as-spun sample (**d**), the formation of Cu-clusters, and the nucleation of nano-scale α-Fe crystals embedded in an amorphous matrix (**e, f**), with an increased volume fraction of these crystals in the H-CL sample (**f**). Line compositional profiles, computed along the sky-blue cylindrical region marked in the respective APT maps of the samples: **g** as-spun, **h** L-CL, **i** H-CL, demonstrate uniform composition in the as-spun sample, with Fe-enriched regions forming in the annealed samples. Error bars indicate the standard deviations of the counting statistics in each bin of the profiles.

magneto-optic Kerr effect (MOKE)[48,49] microscopy, which enables the simultaneous visualization of vector magnetization components with high spatial resolution. Detailed observations of the magnetic domain structures in both static (Fig. 4a–c and Supplementary Fig. 10) and dynamic modes under high AC magnetization fields (Supplementary Movies 1 and 2) revealed an intricate evolution of domain configurations across samples with varying V_f values. In the as-spun amorphous sample, two distinct domain configurations were identified (Fig. 4a): wide and wavy domains with 180° walls aligned along an in-plane direction; and narrow, fingerprint-like domains surrounded by wide lamellar domains. These irregular domain patterns originate from heterogeneous internal stress tensor components[33] generated during rapid quenching. This combination of magnetic domain structure results in high excess losses due to dynamic domain wall displacement under alternating fields. Upon partial nanocrystallization, as seen in the L-CL sample (~5.1% V_f, Fig. 4b), the domain morphology transforms significantly into narrower stripe-shaped domains (4.8 ± 0.6 μm wide), oriented perpendicular to the applied magnetic field. This transformation is attributed to the onset of stress-induced PMA, facilitated by the nucleation of nanoscale α-Fe crystals within the amorphous matrix. PMA stabilizes the domain configuration, suppresses domain wall displacement, and promotes magnetization rotation as the dominant mechanism for magnetization reversal, leading to a remarkable reduction in core loss. The PMA induced in partially nanocrystallized samples likely arises from a synergy of high positive λ_s and compressive internal stresses[33], as quantified using classical domain theory (Supplementary Table 3). The anisotropy energy K, domain wall thickness, and compressive stress were calculated using classical domain theory[34,50] and outlined in Supplementary Table 3. This quantitative analysis reveals that decreasing domain width corresponds to a substantial increase in anisotropy energy, enhancing PMA. With further nanocrystallization (Fig. 4c), the stripe domain width continues to shrink to 2.8 ± 0.2 μm and below 1 μm in samples with 8% and 18% V_f, respectively, corresponding to regions with higher core loss. This refinement of the magnetic domain structure results from an increase in the estimated anisotropy energy due to the increase in internal stress. While strong PMA continues to promote domain refinement, the resulting narrow domains constrain the ease of magnetization rotation and increase total magnetic anisotropy energy, ultimately raising core loss. This highlights a non-monotonic relationship between domain refinement and core loss, while moderate PMA reduces loss, excessive PMA impairs dynamic magnetization processes. Since MOKE observations provide only surface information about the magnetic domain configuration, micromagnetic simulation was employed to gain insight into the 3D magnetization configurations. Given the unknown intrinsic properties values, simulations were conducted with PMA energies ranging from 1 to 20 kJ/m³. The simulation results qualitatively reproduced the experimentally observed surface domain patterns and revealed the volume distribution within the ribbon (Fig. 4d–f). For the as-spun sample, simulations indicate large, curvilinear magnetic domains (Fig. 4d). Introducing a small stress-induced PMA of 5 kJ/m³ transforms the domain structure into alternating stripes perpendicular to the applied magnetic field (H_a) and internal closure domains (Fig. 4e), oriented perpendicular to the applied field. This pattern emerges after relaxing the system from an

initial configuration of two domains along the OY axis, mimicking H_a in the experiment. An increase of the PMA to 20 kJ/m³ further narrows the stripe pattern (Fig. 4f), as domain width is inversely proportional to $(K)^{1/4}$, as detailed elsewhere[50] and qualitatively reproducing the experimentally observed trend of domain refinement with increasing crystallinity.

Under AC magnetic fields, the as-spun sample exhibits magnetization changes primarily driven by domain wall displacement, whereas nanocrystalline samples show limited domain wall motion. This suggests that magnetization changes predominantly occur through magnetization rotation within stripe domains rather than domain wall movement. Due to the narrower stripe magnetic domains, any potential magnetic domain wall motion is significantly slower, as observed in high-frequency dynamic magnetic domain observations (Supplementary Movies 1 and 2), effectively suppressing excess losses. Additionally, the reduction in domain width signifies increased anisotropy energy (Supplementary Table 3), resulting in strong PMA, limiting magnetization rotation and, consequently, increased core loss. Microscopically, as the crystalline volume fraction increases, nanocrystallites form interconnected α-Fe networks separated by an iron-lean amorphous matrix. This morphology is known to enhance coercivity through mechanisms as described in simulations of random magnetic anisotropy[51] and magnetostriction in randomly oriented nanocrystallites[45]. However, the coercivity remains nearly constant in the present case, likely due to the nanoscale size of the crystallites below the domain wall width and their homogeneous distribution, which effectively suppresses domain wall pinning. As the domain width shrinks due to stronger PMA, the dominant magnetization reversal mechanism changes from domain wall motion to coherent rotation. However, beyond an optimal V_f range, the associated increases in anisotropy energy outweigh the benefits, leading to higher core loss despite reduced domain wall mobility. While this study outlines the essential physics linking nanocrystallization, domain configuration, and dynamic magnetization behavior, the detailed mechanisms underlying these phenomena require further theoretical exploration. Future work integrating micromagnetic and phase-field simulations could provide deeper insights into the coupling between structural evolution and magnetic dynamics. Overall, this study establishes a clear design strategy for reducing the high-frequency core loss and highlights the potential for optimizing existing soft magnetic materials through nanostructure and domain engineering, aiming to fully harness their capabilities by refining domain structure and controlling the magnetization process.

The study examines the soft magnetic behavior of Fe-enriched ribbons tailored by nanostructure-domain engineering, demonstrating excellent ultra-low core loss at high-frequency regions. The proposed and demonstrated concept of magnetic domain engineering for high-frequency application toward the reduction of core loss can be extended to all amorphous magnetic ribbons having high λ_s values[28,30,44], as shown in Fig. 5a. Interestingly, partially nanocrystallized ribbons consistently showed lower core loss, validating the effectiveness and universality of our approach. While conventional design strategies favor very low or near-zero λ_s to suppress magnetoelastic energy and minimize loss, our results
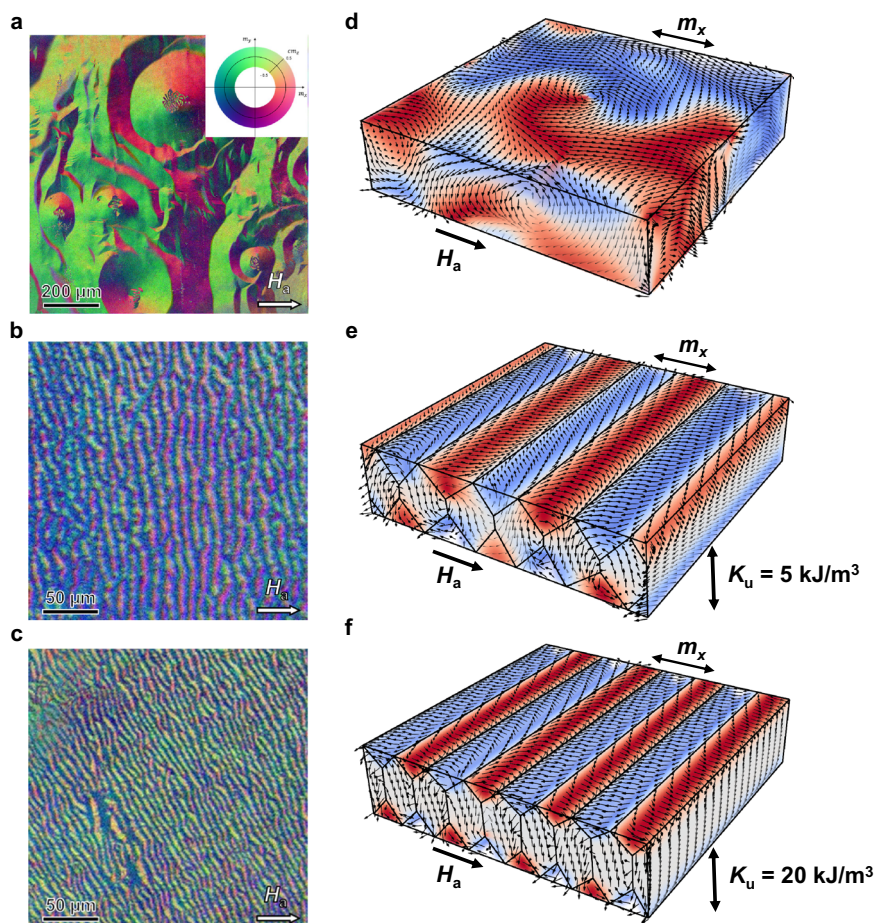
Fig. 4 | Magnetic domain structure of Fe-enriched soft magnetic ribbons. The magnetic domain structure at remanence for samples in different conditions: **a** as-spun ribbon, and with varying crystalline volume fraction V_f of **b** 5.1% (L-CL), and **c** 8%. The magnetic domain images are displayed in pseudo-colors, with the x, y, and z components of the magnetization vector assigned to red, green, and blue, respectively. Simulated domain patterns with **d** wavy and curled domains, **e** stripe domains perpendicular to the H_a field indicating weak stress-induced PMA with K_u ~ 5 kJ/m³, and **f** closure stripe domains with a higher K_u ~ 20 kJ/m³ value, with a noticeable reduction in stripe width.

reveal a maintaining a relatively high λ_s is instrumental in tailoring the magnetic domain structure and magnetization process for ultra-low core loss. This concept opens new avenues and expands the material space by developing ultra-low core loss soft magnetic materials while maintaining a large λ_s. The developed ultra-low core loss ribbons exhibit a remarkable combination of low H_c (~4 A/m), moderately high $\mu_0 M_s$ (~1.61 T), high ρ (~1.56 μΩm), and an extremely low P_T (~75 ± 1.3 W/kg at 10 kHz, 1 T) with a substantial λ_s value of 31 ppm. Although high core loss ribbons show a higher P_T value of 140 ± 0.4 W/kg, still achieve a notably high $\mu_0 M_s$ value of 1.76 T, demonstrating the trade-off between magnetization and loss performance. The observed ~13% lower $\mu_0 M_s$ and ~200% higher λ_s (Fig. 2a–c) for the partially nanocrystallized sample arise from its limited volume fraction of high-magnetization α-Fe nanocrystals and the dominant amorphous matrix contribution, which intrinsically possesses a high positive λ_s. The increased λ_s, in conjunction with internal compressive stresses, promote the establishment of weak PMA, facilitating the formation of narrow stripe-shaped magnetic domains. This domain configuration effectively suppresses dynamic domain wall motion and significantly reduces excess loss at high frequencies. The elevated λ_s can also amplify magnetoelastic energy, potentially leading to mechanical fatigue or increased noise under dynamic conditions. However, in our study, the crystalline volume fraction is carefully controlled (V_f = 1–6%), which likely mitigates these detrimental effects. Furthermore, the amorphous matrix provides mechanical damping and flexibility, reducing the

probability of structural degradation under cyclic loading. From an application perspective, the slight reduction in $\mu_0 M_s$ (~1.61 T) moderately lowers the maximum achievable energy density but remains sufficiently high to meet the demands of compact and high-power-density magnetic devices. This underscores the strategic advantage of partial nanocrystallization in balancing magnetic softness, energy density and frequency performance. Furthermore, to evaluate the robustness and sensitivity of our process, we conducted additional control experiments using a lower heating rate of 20 K/min and extended annealing durations. The effects of these conditions on microstructure and magnetic properties are illustrated in Supplementary Fig. 11. These slower thermal cycles produced nanocrystalline structures with ultra-low core loss (~72 W/kg at 1 T, 10 kHz), demonstrating the tunability and versatility of our approach. To assess industrial applicability, we evaluated the $\mu_0 M_s$ and P_T of commercial Fe-based soft magnetic materials under identical conditions and compared them with our materials (Fig. 5b). This reveals a significant breakthrough, as the developed materials in this study outperform existing materials by demonstrating the lowest P_T alongside a high $\mu_0 M_s$ value. Additionally, the partial crystallization of α-Fe within the amorphous matrix retains moderate flexibility, highlighting the effectiveness and superior performance of our approach. This advancement holds significant potential for energy-efficient technologies and advanced magnetic systems, positioning these materials as leading contenders in the soft magnetic industry.
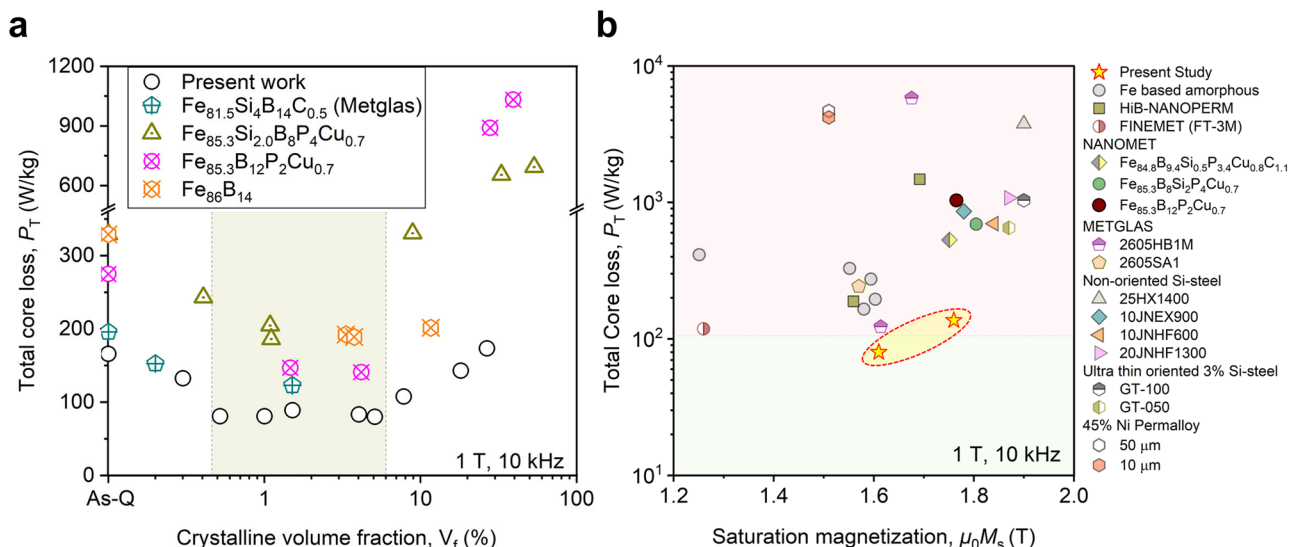
Fig. 5 | Validation of the proof-of-concept and comparisons of core loss and saturation magnetization in Fe-based soft magnetic materials. a Validation of the proposed approach through nanostructure engineering applied to other Fe-based amorphous ribbons containing high magnetostriction values. Notably, core loss reduction is observed for the partially nanocrystallized ribbons. **b** Comparison of the core loss P_T and saturation magnetization $\mu_0 M_s$ among various Fe-based soft magnetic materials measured under identical conditions. The newly developed Fe-enriched ribbons with partial nanocrystallization demonstrate the lowest P_T and moderately high $\mu_0 M_s$, outperforming commercially available Fe-based soft magnetic materials.

This study proposes and demonstrates a novel strategy to achieve ultra-low core loss at elevated frequencies in Fe-based soft magnetic ribbons by integrating nanostructures and magnetic domain engineering. Partial nanocrystallization of α-Fe with V_f ranging up to 6% within a residual amorphous matrix enabled us to establish PMA, forming a narrow stripe-pattern domain structure that remarkably reduced core losses by 55%, predominantly the excess loss. We have demonstrated that the ultra-low core loss is realized by controlling the rotation of magnetization at high frequencies, realized in an optimum PMA range in the materials. Additionally, the proposed alloy design holds broad potential for various systems through the development of nanocomposite materials with tailored domain structures. Furthermore, the ability to engineer stripe-shaped magnetic domains through controlled partial nanocrystallization, despite a moderate increase in magnetostriction, positions these materials as promising candidates for high-frequency applications where minimizing dynamic core losses outweighs concerns related to magnetoelastic effects. This opens new avenues for the development of advanced soft magnetic materials with ultra-low core losses, enabling energy-efficient and miniaturized power electronics for modern applications. Future research can focus on developing materials with high saturation magnetization and minimal core loss using this novel approach, alongside comprehensive computational analysis of core loss mechanisms to enhance material performance.

Methods

A master alloy ingot was prepared using vacuum induction melting under an Ar atmosphere, with the addition of high-purity elements of Fe (99.99 %), Si (99.99%), Cu (99.9%), B (99.5%), and Fe_3P (99%). The as-cast ingot was subsequently employed to fabricate Fe-enriched amorphous ribbons with a chemical composition of $Fe_{84.8}Si_{0.5}B_{9.4}P_{3.4}Cu_{0.8}C_{1.1}$ (in at.%). These ribbons were produced on an industrial scale by M/s Tohoku Magnet Institute Co. Ltd using the melt-spinning technique, yielding high-quality amorphous ribbons with lengths extending to several hundred meters, widths of 60 mm, and consistent thicknesses of $25 \pm 1\,\mu m$ (Supplementary Fig. 1). For thermal processing, the ribbons were cut to the desired dimensions required for measurements, then wrapped in Ta foil and

sandwiched between two stainless steel (SUS) sheets for uniform heat distribution. The samples were annealed in direct contact with the heater at high heating rates of 5.83 K/s, with a short soak time of around 4 s at various temperatures (Supplementary Table 1). The accuracy of temperature measurements was confirmed using K-type thermocouples. This thermal treatment was carefully designed to generate diverse microstructural features.

The chemical composition of the ribbons was analyzed using inductively coupled plasma optical emission spectrometry (ICP-OES). DSC (Perkin Elmer DSC8500) was performed at a heating rate of 40 K/min under an Ar flow to study the thermal properties of the as-spun ribbon. XRD (Rigaku MiniFlex600), using Cu-Kα radiation, was employed to examine the structure characteristics, with crystallite sizes estimated from the XRD peak broadening using the Scherrer equation[52]. Samples with crystallite sizes below 20 nm were selected for the present study. The XRD data were analyzed employing a pseudo-Voigt peak profile fitting function to distinguish between amorphous and crystalline phases. The volume fraction of the crystalline phase was determined by comparing the integral intensity of the crystalline peaks to the total intensity. Additionally, the strain associated with the formation of the crystalline phase was estimated using the Williamson–Hall method, with a particular focus on the α-Fe crystalline peaks. Microstructural analysis was performed using a transmission electron microscope (TEM, FEI Titan G^2 80–200) equipped with a probe corrector. The three-dimensional elemental distributions were obtained through atom probe tomography (APT) utilizing the CAMECA LEAP 5000 XS instrument operated in the pulsed laser mode at a repetition rate of 250 kHz. The laser pulse energy was set at 30 pJ, and the experiments were carried out at a specimen temperature of 30 K, maintaining a constant detection rate of 1.5%. The obtained APT data were subsequently analyzed using CAMECA AP Suite 6.3 software. The TEM specimens and APT tips were prepared from the center of the ribbons by lift-out and annular milling techniques using a dual beam-focused ion beam (FEI Helios 5UX) techniques, with final ion milling performed at low-energy (5 keV) Ga beam to prevent damage.

The magnetic domain structure was analyzed in static and dynamic mode by a self-made stroboscopic time-resolved MOKE microscope using pulsed semiconductor lasers as a light source[48,49]. This system enables the acquisition of high-resolution vector magnetic domain images by combining multiple magnetic domain images taken at different illumination directions. The use of a pulsed semiconductor laser as an illumination source enables stroboscopic time-resolved observation in the kHz–MHz frequency range. The air-side surface of the melt-spun ribbons is optically smooth, permitting direct examination of the domains without polishing the ribbons. Dynamic observations were conducted on a ribbon sample shaped into a ring with an outer diameter of 30 mm and an inner diameter of 20 mm, which was wound with a 10-turn excitation coil. The striped magnetic domains observed are produced when the applied magnetic field is reduced after saturating the magnetization with a field aligned along the H_a direction (indicated in Fig. 4). Dynamic magnetic domain images are captured using an AC magnetic field applied in the H_a direction, while static magnetic domain images are obtained in a remanent state. Micromagnetic simulations were performed to analyze the three-dimensional magnetic domain configurations. The simulated geometry measured $648 \times 648 \times 162\,nm^3$, with a simulation cell size of $2 \times 2 \times 2\,nm^3$, and periodic boundary conditions were applied within the ribbon plane. Due to the small model size, we reduced exchange stiffness A from 5 pJ/m to 1 pJ/m, which allowed us to obtain qualitatively similar magnetic domain patterns. The total energy considered in the simulations included magnetostatic, exchange, and stress-induced out-of-plane uniaxial anisotropy terms. The micromagnetic software MuMax3 was utilized to solve the Landau–Lifshitz–Gilbert equation and determine the equilibrium magnetic state[53].

The saturation magnetization and coercivity were measured using a vibrating sample magnetometer (LakeShore VSM 740) with a maximum applied magnetic field of 1 T on a circular specimen with a diameter of 6 mm. Multiple samples were taken to improve the statistical reliability of the data. Coercivity was further validated with a DC B-H loop tracer (Riken Denshi BHS-40) using a solenoidal coil at a maximum applied magnetic field of 2 kA/m. Hysteresis measurements were conducted in an Epstein frame to eliminate demagnetization effects. Magnetostriction measurements were carried out using a custom-made magnetostriction measurement device for ribbons (Toei Science Industry Co. Ltd.). Strain gauges were attached to both sides of the ribbon, and the saturation magnetostriction was measured with an external magnetic field applied via a Helmholtz coil, with a maximum field of 30 mT.

Total core losses P_T were estimated using rectangular samples with 10 mm width and 70 mm length. An AC BH analyzer (Iwatsu SY-8219 and SY-956) was employed at a magnetic flux density of 1 T and a frequency of 10 kHz. The losses were categorized into sub-components, i.e., hysteresis loss P_h, classical eddy current loss P_e, and excess loss, P_a, using a conventional empirical model. The P_h was calculated using the Steinmetz hysteresis loss model[15,30] and represented as

$$P_h = k_h B_m^n f$$

The hysteresis loss coefficient, k_h, and the exponent n related to the B_m were evaluated through least square fitting of the loss per cycle (Pcyc) curve measured at different B_m values in a DC magnetic field. The P_h values were estimated by multiplying the frequency f by the area of the DC hysteresis loop ($k_h B_m^n$), measured using the BHS-40. The P_e was derived from Maxwell's equation as given below[15,30,39]

$$P_e = \frac{\pi^2 t^2 B_m^2 f^2}{6\rho\sigma}$$

where t represents the thickness of the ribbons and σ denotes the density (=7.45 g/cm^3). P_a was determined by subtracting P_h and P_e from the measured total core loss (P_T).

Broadband complex permeability and core loss per circle P_c of both as-spun and low core loss samples annealed at 698 K (L-CL) were measured across a range of B_m from 1 mT to 500 mT. These measurements were performed for the frequency range from 10 Hz to 5 MHz using a B-H analyzer (IWATSU SY-8218). Accurate data for P_c and permeability are critical for applying the magnetization process decomposition model. The accuracy of P_c measurement for each technique was thoroughly verified using the R_0 plot method[53], where R_0 represents the low B_m limit of equivalent resistance of core loss, defined as $R = P_c f/I_m^2$, and I_m is the input current amplitude. The broadband relative initial complex permeability spectra (μ' and μ'') of the samples were obtained using an impedance analyzer (KEYSIGHT E4990).

Data availability
The data that support the findings of this study are available from the corresponding author upon reasonable request.

References
1. Zhou, L. & Preindl, M. Variable switching frequency techniques for power converters: review and future trends. *IEEE Trans. Power Electron.* **38**, 15603–15619 (2023).
2. Neumayr, D. The essence of the little box challenge-part B: hardware demonstrators & comparative evaluations. *CPSS Trans. Power Electron. Appl.* **5**, 251–272 (2020).
3. Silveyra, J. M., Ferrara, E., Huber, D. L. & Monson, T. C. Soft magnetic materials for a sustainable and electrified world. *Science* **362**, 418 (2018).
4. Talaat, A., Greve, D. W., Suraj, M. V. & Ohodnicki, P. R. Electromagnetic assisted thermal processing of amorphous and nanocrystalline soft magnetic alloys: fundamentals and advances. *J. Alloy. Compd.* **854**, 156480 (2021).
5. Han, L. et al. A mechanically strong and ductile soft magnet with extremely low coercivity. *Nature* **608**, 310–316 (2022).
6. Han, L. et al. Strong and ductile high temperature soft magnets through Widmanstätten precipitates. *Nat. Commun.* **14**, 8176 (2023).
7. Ouyang, G. et al. Near net shape fabrication of anisotropic Fe-6.5% Si soft magnetic materials. *Acta Mater.* **201**, 209–216 (2020).
8. Krings, A., Boglietti, A., Cavagnino, A. & Sprague, S. Soft magnetic material status and trends in electric machines. *IEEE Trans. Ind. Electron.* **64**, 2405–2414 (2017).
9. Hilzinger, R. & Rodewald, W. *Magnetic Materials: Fundamentals, Products, Properties, Applications* (VAC Vacuumschmelze, 2013).
10. Toshito, T., Kazuhiro, H. & Takehiro, S. *Recent Development of Grain-Oriented Electrical Steel in JFE Steel. JFE Technical Report* vol. 21 (2016).
11. Jahangiri, M. R., Bayani, H., Ardestani, M. & Mehdizadeh, M. Core loss reduction in grain oriented silicon steel sheets by two-sided laser scribing in the presence of a magnetic field. *J. Alloy. Compd.* **891**, 162080 (2022).
12. Iuchi, T. et al. Laser processing for reducing core loss of grain oriented silicon steel. *J. Appl. Phys.* **53**, 2410–2412 (1982).
13. Tumanski, S. Modern magnetic materials—the review. *Prz. Elektrotech.* **86**, 1–15 (2010).
14. Gautam, R., Prabhu, D. B., Chandrasekaran, V., Gopalan, R. & Sundararajan, G. Influence of nanoprecipitates, solid solution and grain size on the magnetic and electrical properties of Fe-P-Si alloys. *J. Magn. Magn. Mater.* **493**, 165743 (2020).
15. Gautam, R. et al. Effect of recovery and recrystallization on microstructure and magnetic properties of Fe-0.4P rolled sheets. *Materialia* **13**, 100863 (2020).

16. Shokrollahi, H. & Janghorban, K. Soft magnetic composite materials (SMCs). *J. Mater. Process. Technol.* **189**, 1–12 (2007).

17. Yoshizawa, Y., Oguma, S. & Yamauchi, K. New Fe-based soft magnetic alloys composed of ultrafine grain structure. *J. Appl. Phys.* **64**, 6044–6046 (1988).

18. Suzuki, A., Makino, A., Kataoka, N., Inoue, A. & Masumoto, T. High saturation magnetization and soft magnetic properties of bcc Fe–Zr–B and Fe–Zr–B–M (M=Transition Metal) alloys with nanoscale grain size. *Mater. Trans. JIM* **32**, 93–102 (1991).

19. Naitoh, Y. et al. Applications of nanocrystalline soft magnetic Fe-M-B (M = Zr, Nb) alloys. *Nanostruct. Mater.* **8**, 987–995 (1997).

20. Herzer, G. Modern soft magnets: amorphous and nanocrystalline materials. *Acta Mater.* **61**, 718–734 (2013).

21. Herzer, G. Nanocrystalline soft magnetic materials. *J. Magn. Magn. Mater.* **157–158**, 133–136 (1996).

22. Urata, A., Matsumoto, H., Yoshida, S. & Makino, A. Fe-Si-B-P-Cu Nanocrystalline alloy ribbons with high saturation magnetic flux density prepared using industrial materials. *IEEE Trans. Magn.* **47**, 3177–3179 (2011).

23. Urata, A., Yamaki, M., Satake, K., Matsumoto, H. & Makino, A. Magnetic properties and structure of $Fe_{83.3–85.8}B_{7.0–4.5}Cu_{0.7}P_9$ nanocrystalline alloys. *J. Appl. Phys.* **311**, 17A311 (2013).

24. Takenaka, K., Nishijima, M. & Makino, A. Effect of metalloid elements on the structures and soft magnetic properties in $Fe_{85.2}Si_xB_{14-x-y}P_yCu_{0.8}$. Alloy. *IEEE Trans. Magn.* **50**, 13–16 (2014).

25. Setyawan, A. D. et al. Magnetic properties of 120-mm wide ribbons of high Bs and low core-loss NANOMET® alloy. *J. Appl. Phys.* **117**, 17B715 (2015).

26. Parsons, R., Li, Z. & Suzuki, K. Nanocrystalline soft magnetic materials with a saturation magnetization greater than 2. *T. J. Magn. Magn. Mater.* **485**, 180–186 (2019).

27. Suzuki, K. et al. Nanocrystalline soft magnetic materials from binary alloy precursors with high saturation magnetization. *AIP Adv.* **9**, 035311 (2019).

28. Dastanpour, E., Enayati, M. H., Masood, A. & Ström, V. Quantification of the anomalous crystallization and soft magnetic properties of Fe–Si–B–P–Cu (Nanomet) by isothermal calorimetry. *J. Alloy. Compd.* **830**, 154705 (2020).

29. Suzuki, K. Recent advances in nanocrystalline soft magnetic materials: a critical review for way forward. *J. Magn. Magn. Mater.* **592**, 171677 (2024).

30. Pry, R. H. & Bean, C. P. Calculation of the energy loss in magnetic sheet materials using a domain model. *J. Appl. Phys.* **29**, 532–533 (1958).

31. Ono, N. et al. Analysis on iron loss of sendust dust cores based on magnetization reversal processes. *IEEE Trans. Magn.* **59**, 1–5 (2023).

32. Hubert, A. & Schafer, R. *Magnetic Domains: The Analysis of Magnetic Microstructures* vols 366–368 (Springer, 2009).

33. Kronmüller, H. et al. Magnetic properties of amorphous ferromagnetic alloys. *J. Magn. Magn. Mater.* **13**, 53–70 (1979).

34. Ok, H. N. & Morrish, A. H. Origin of the perpendicular anisotropy in amorphous Fe82B12Si6 ribbons. *Phys. Rev. B* **23**, 2257–2261 (1981).

35. Salzmann, P., Grimm, W. & Hubert, A. Anisotropies and domain structures in metallic glasses. *J. Magn. Magn. Mater.* **31–34**, 1599–1600 (1983).

36. Loffler, P., Wengerter, R. & Hubert, A. Experimental and theoretical analysis of 'stress pattern' magnetic domains in metallic glasses. *J. Magn. Magn. Mater.* **41**, 175–178 (1984).

37. Dijkstra, L. J. & Wert, C. Effect of inclusions on coercive force of iron. *Phys. Rev.* **79**, 979–985 (1950).

38. Bertotti, G. A general statistical approach to the problem of eddy current losses. *J. Magn. Magn. Mater.* **41**, 253–260 (1984).

39. Bertotti, G. Connection between microstructure and magnetic properties of soft magnetic materials. *J. Magn. Magn. Mater.* **320**, 2436–2442 (2008).

40. Ono, N. et al. Multimodal iron loss analyses based on magnetization processes for various soft magnetic toroidal cores. *J. Magn. Magn. Mater.* **603**, 172222 (2024).

41. Sharma, P., Zhang, X., Zhang, Y. & Makino, A. Influence of microstructure on soft magnetic properties of low coreloss and high Bs $Fe_{85}Si_2B_8P_4Cu_1$ nanocrystalline alloy. *J. Appl. Phys.* **115**, 17A340 (2014).

42. Abo, G. S. et al. Definition of magnetic exchange length. *IEEE Trans. Magn.* **49**, 4937–4939 (2013).

43. Tsukahara, H., Huang, H., Suzuki, K. & Ono, K. Formulation of energy loss due to magnetostriction to design ultraefficient soft magnets. *NPG Asia Mater.* **16**, 19 (2024).

44. Tsukahara, H., Imamura, H., Mitsumata, C., Suzuki, K. & Ono, K. Role of magnetostriction on power losses in nanocrystalline soft magnets. *NPG Asia Mater.* **14**, 44 (2022).

45. Suzuki, K. et al. Copper-free nanocrystalline soft magnetic materials with high saturation magnetization comparable to that of Si steel. *Appl. Phys. Lett.* **110**, 012407 (2017).

46. Gautam, R. et al. Creation of flexible spin-caloritronic material with giant transverse thermoelectric conversion by nanostructure engineering. *Nat. Commun.* **15**, 1–9 (2024).

47. Ogasawara, T. Improvement in spatial frequency characteristics of magneto-optical Kerr microscopy. *Jpn. J. Appl. Phys.* **56**, 108002 (2017).

48. Ogasawara, T. & Yamaguchi, A. Observation of frequency dependent resonances in magnetic vortex core gyration using time-resolved magneto-optical Kerr microscope with pulsed semiconductor laser illumination. *Jpn. J. Appl. Phys.* **61**, 018001 (2022).

49. Kittel, C. Theory of the structure of ferromagnetic domams in films and small particle. *Phys. Rev.* **70**, 965–971 (1946).

50. Lee, S.-J., Sato, S., Yanagihara, H., Kita, E. & Mitsumata, C. Numerical simulation of random magnetic anisotropy with solid magnetization grains. *J. Magn. Magn. Mater.* **323**, 28–31 (2011).

51. Cullity, B. D. *Elements of X-Ray Diffraction* (Addison-Wesley Publishing Company, Inc., 1956).

52. Vansteenkiste, A. et al. The design and verification of MuMax3. *AIP Adv.* **4**, 107133 (2014).

53. Sato, Y. et al. Accuracy investigation of high-frequency core-loss measurement for low-permeability magnetic materials. *IEEE Trans. Magn.* **59**, 6301105 (2023).

Acknowledgements

Author contributions

R.G. and H.S.A. conceived the research idea, R.G., S.H., and H.S.A. designed experiments, R.G., H.S.A., and T.O. conducted the microstructural characterization. R.G., H.M., and S.H. conducted the magnetic measurements, S.H. and T.O. conducted MOKE, N.K. performed the simulation study, S.O. and N.O. performed the broadband permeability experiments, R.G. collected and analyzed the data. All authors discussed the results and contributed to the preparation and revision of the manuscript.

Competing interests

The authors declare no competing interests.

Additional information

Supplementary information The online version contains supplementary material available at
https://doi.org/10.1038/s41467-025-63139-1.

Correspondence and requests for materials should be addressed to Hossein Sepehri-Amin.

Reprints and permissions information is available at
http://www.nature.com/reprints

Publisher's note Springer Nature remains neutral with regard to jurisdictional claims in published maps and institutional affiliations.